2010 IEEE International Conference on Robotics and Automation
Anchorage Convention District
May 3-8, 2010, Anchorage, Alaska, USA

Model-Based Control of a High-Precision Imprinting Actuator for Micro-Channel Fabrications

Tat Joo Teo, *Member; IEEE*, I-Ming Chen, *Senior Member; IEEE*,
Choon Meng Kiew, *Member; IEEE*, Guilin Yang, *Member; IEEE* and Wei Lin, *Member; IEEE*

***Abstract*— This paper presents the modeling and control of a Flexure-Based Electromagnetic Linear Actuator (FELA) that is employed as a high-precision imprinting actuator of a desktop hot-embossing imprinter. In this work, a systematic approach of obtaining the unknown physical parameters of FELA is presented. Subsequently, these parameters are used to design two model-based PID controllers that allow the FELA to perform high-precision positioning tasks and direct-force imprinting tasks respectively. As the imprinting tasks require the FELA to operate in both position and direct-force control modes, two types of control strategies are explored and their competency of enabling the FELA to perform such tasks are investigated. Lastly, the selected control strategy is implemented on the FELA to assist the hot-embossing imprinter in fabricating micro-channels on polymer substrates via a hot-embossing process.**

I. INTRODUCTION

The transfer of high-resolution features through mechanical pressing has recently become a promising approach in achieving high-throughput fabrication of polymer-based devices such as optical components and micro-fluidic devices etc. This approach physically imprints the pre-fabricated features from the molds (or templates) onto the polymer substrates and uses either the thermal forging (termed hot-embossing process) or the Ultra-Violet (UV) curing (termed UV-embossing process) to complete the formation of the imprinted features. To investigate the deformation behavior of the polymer substrate during hot-embossing, Kiew et al [1] proposed a mathematical model to simulate the behavior of a polymer material, i.e., PolyMethyl-MethAcryle (PMMA), during a hot-embossing process. Unlike conventional simulation approaches, which use the Mooney-Rivlin model [2], this approach allows the use of fundamental material properties directly and achieves more realistic simulations of those polymer behavioral.

The promising results from this proposed simulation approach have led to the development of a desktop hot-embossing imprinter for evaluating the proposed simulation approach via conducting actual process studies. In this imprinter, the desired imprinting actuator must have a small footprint due to the proposed desktop package. In addition, this actuator must provide a continuous output force of at least 100 N for rapid small scale imprinting, and a few millimeters of displacement stroke for demolding or assessing the substrates. Most importantly, it must offer high-precision positioning and direct-force control capabilities for accurate and repeatable process studies on micro-scale feature fabrications through the hot-embossing process.

Unfortunately, most existing actuators have limitations in meeting all those requirements. Conventional hydraulic actuators offer high output force but are bulky in size and have poor force control resolution due to the compressive nature of fluid. Similarly, the linear-stepper motors are unable to provide positioning and direct-force control although large output force are expected. In addition, the voice-coil actuators produce small output forces [3] while the force generation of the solenoid actuators are inconsistent and nonlinear [4]. On the other hand, piezoelectric actuators may be capable of achieving high-precision resolutions but have limited displacement of up to several hundred microns [5]. Although such limitations can be overcome through techniques such as the magnetostrictive clamping [6], the inchworm clamping [7], and the impact-force method [8] etc, low payload capacity, slow response speed and poor repeatable motion are the common trade-offs.

II. OBJECTIVES

Due to the limitations of existing actuators, a novel nano-positioning actuator, termed Flexure-Based Electromagnetic Linear Actuator (FELA), is employed as the imprinting actuator for the proposed system. It mainly comprises of a Lorentz-force Electromagnetic (EM) module and flexure-based support bearings as shown in Fig. 1 [9]. Currently, FELA is able to achieve a positioning accuracy of ± 10 nm over a displacement stroke of 4 mm, and a continuous output force of 60 N/Amp with an accuracy of ± 0.15 N [10]. In this work, the FELA must be able to transit between the position and the direct-force control modes. Consequently, an accurate modeling of the system and a proper control strategy are required to realize the imprinting process. Hence, this paper focuses on the design and modeling of the model-based controllers for the FELA, and investigates the control strategies that will be used to realize the transition between both control modes. With the selected control strategy, FELA is implemented in the proposed system to realize the imprinting of micro-sized channels through a hot-embossing process. Experimental results obtained from the imprinted features will also be discussed.

This work fully funded and supported by Singapore Institute of Manufacturing Technology (SIMTech)

T. J. Teo, C. M. Kiew, G. L. Yang and W. Lin are with Mechatronics Group, SIMTech, 71 Nanyang Drive, Singapore 638075, tjteo@SIMTech.a-star.edu.sg

I. -M. Chen is with School of Mechanical and Aerospace Engineering, Nanyang Technological University, 50 Nanyang Avenue, Singapore 639798 michen@ntu.edu.sg

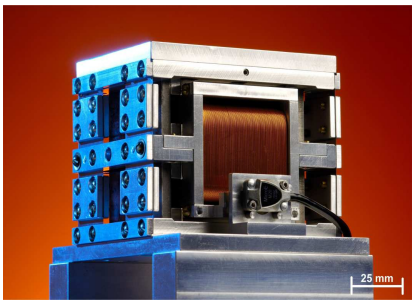

Fig. 1. FELA prototype.

III. Hybrid Position/Force Control Strategy

Two control schemes are investigated to realize the transition of the FELA between the positioning control and the direct-force control.

A. Mode-Switching

The first scheme is the mode-switching control. It allows the FELA, which is operating in a position control mode, to switch to a direct-force control mode when a contact force at the tip of the actuator is detected. This scheme performs two control-loops, i.e., the position control and the direct-force control, simultaneously and switches between both control-loops with respect to varying conditions. Fig. 2 illustrates the block diagram of the proposed mode-switching control scheme whereby two separate Proportional-Integral-Derivative (PID) controllers are implemented to control the positioning and output force of the FELA respectively.

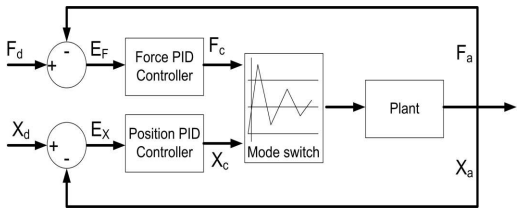

Fig. 2. Block diagram of the proposed mode-switching control scheme.

B. Impedance Control

The second scheme adopts an impedance control that performs a position control loop initially before inheriting the command signals from a direct-force control loop when a contact force is detected at the actuator tip. Once a contact force is detected, the inherited command signals of the direct-force control loop dominate the command signals of the position control loop. Eventually, the command signals sent to the FELA will be provided by the direct-force control loop. Fig. 3 illustrates the block diagram of the proposed impedance control scheme.

IV. Model-Based PID Controller

In both proposed control schemes, two separate sets of PID parameters are used to realize the positioning control mode and the direct-force control mode. Prior to the implementation of both control schemes, the PID controllers need

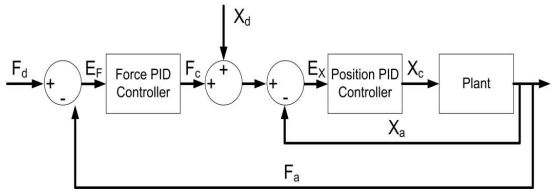

Fig. 3. Block diagram of the proposed impedance control scheme.

to be designed. In previous effort [10], the entire system was treated as a black-box system and MATLAB *System Identification Toolkit* was used to predict the transfer function of the plant. However, the predicted transfer function is just a mathematical expression that has no relationship with the physical parameters of the plant. In this work, the transfer function of the plant is modeled through these physical parameters and the PID controllers are designed based on the modeled transfer function.

A. Position PID Controller Design

For the position controller, the feedback loop is formed by a linear optical encoder from MicroE-System (model: M3500). Fig. 4a shows the block diagram of a basic position closed-loop control system where $G_{Cp}(s)$ represents the position PID controller and $G_{Fp}(s)$ represents the FELA. For position control, a FELA is treated as a linear mass-spring-damper system as shown in Fig. 4b whereby the mass, m, represents the weight of the moving air-core coil, the stiffness, k, represents the stiffness of the flexure-based support bearings, and the damper, b, represents the passive eddy current damping inherited from the motion between the moving coil and the magnets within the EM module.

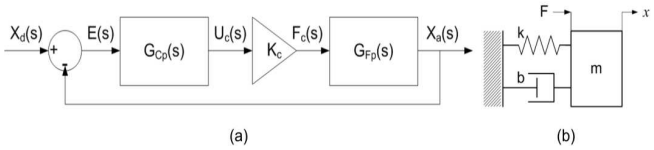

Fig. 4. (a) Block diagram of the proposed positioning control system with FELA represented as (b) a mass-spring-damper system.

Based on Fig. 4a, the transfer function of the entire closed-loop control system is

$$\frac{X_a(s)}{X_d(s)} = \frac{K_c K_p (T_d s^2 + s + T_i^{-1})}{ms^3 + (b + K_c K_p T_d)s^2 + (k + K_c K_p)s + K_c K_p T_i^{-1}} \quad (1)$$

where $X_a(s)$ represents the actual position, $X_d(s)$ represents the desired position, K_c represents the compensation gain, K_p represents the proportional gain, T_i represents the integral time, and T_d represents the derivative time.

To determine the control parameters, (1) is compared against the transfer function of a standard third-order system so as to formulate the relevant equations that represent K_p, T_i and T_d. The transfer function of a standard third-order system is derived by adding an additional pole to the

transfer function of a standard second-order system. The value of the additional pole must be at least 5 times the value of an undamped natural frequency to ensure that it has minimal effect on the system characteristic. Hence, the transfer function of a standard third-order system is

$$G(s) = \frac{\omega_n^2}{(s+\gamma)(s^2+2\zeta\omega_n s+\omega_n^2)} \tag{2}$$

where ω_n represents the undamped natural frequency of the control system, ζ represents the damping ratio of the control system, and γ represents the additional real pole.
Based on past literature [12], the undamped natural frequency, which is expressed by the desired rise time, T_r, and ζ, is given as

$$\omega_n = \frac{\tan^{-1}[\zeta^{-1}(\sqrt{1-\zeta^2})]}{T_r\sqrt{1-\zeta^2}} \tag{3}$$

A comparison between the coefficients of (1) and (2) yields

$$K_p = \frac{m(\omega_n^2+2\zeta\omega_n\gamma)-k}{K_c} \tag{4}$$

$$T_i = \frac{K_c K_p}{m\gamma\omega_n^2} \tag{5}$$

$$T_d = \frac{m(\gamma+2\zeta\omega_n)-b}{K_c K_p} \tag{6}$$

To determine the PID control parameters through (4) to (6), the values of m, k, b, T_r, and ζ are required. In this work, the mass of the moving coil is measured before assembling the FELA, the stiffness of the flexure-based support bearings is determined experimentally and analytically [11], the rise time is based on the desired value, and the damping ratio of the control system is based on the ideal value. Through these measurements, the values of several control parameters are obtained, i.e., m = 0.5 Kg, k = 2000 N/m, T_r = 0.002 sec, and ζ = 0.76.

In this work, the passive eddy current damping and the compensation gain are determined through an empirical approach. Initially, an open-loop step response is obtained from the FELA. Subsequently, the output and input are recorded at a sampling time of 10 msec. The input is the PC command and the output is in encoder count. The ratio of the recorded output and the input is equivalent to the dc gain of the control system. Based on (1), this dc gain can also be expressed as

$$DC_{gain} = \frac{K_c}{k} \tag{7}$$

Hence, the compensation gain of the entire control system is obtained through the experimental results and (7). This compensation gain accounts for the quantization from the PC command to the FELA position output in encoder count of the open-loop control system. Based on Fig. 4, the transfer function of the open-loop system for FELA is given as

$$G_{Fp}(s) = \frac{K_c}{ms^2+bs+k} \tag{8}$$

Based on (8), the output of this transfer function is plotted against the recorded open-loop step response. Subsequently, the value of the passive eddy current damping was constantly altered to fit the output of the transfer function to match the recorded open-loop step response as shown in Fig. 5.

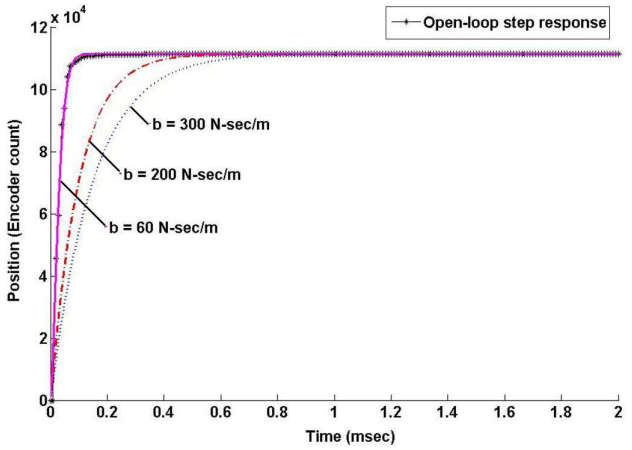

Fig. 5. Open-loop step response and the output of (8) due to the different values of the passive eddy current damping.

From this empirical approach, it shows that a small passive eddy current damping is present in the open-loop system as the output of the transfer function begins to match the actual open-loop step response when the passive damping is reduced. From Fig. 5, both data matches when the passive eddy current damping of the FELA is predicted at 60 N-sec/m. In addition, the compensation gain of the control system is found to be 2.228×10^6 using (7). Finally, these parameters are substituted into (4) to (6) to determine the PID parameters for the positioning control of the FELA.

B. Direct-Force PID Controller Design

A six-axes Force/Torque (F/T) sensor from ATI (model: MINI40) is used as the force feedback encoder to form the closed-loop control system for the FELA to perform a direct-force control (Fig. 6a). In this work, only one axis (Z-axis) is used as the feedback while the remaining axes are used to monitor the surface alignment between the mold and the substrate during the imprinting process. Nevertheless, the entire F/T sensor is treated as a linear spring-damper system where the spring stiffness, k_s, represents the stiffness of the strain gauge within the F/T sensor while the damper, b_s, represents the friction between the F/T sensor and the workpiece.

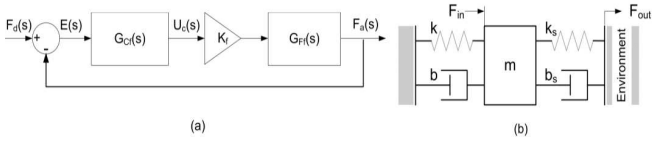

Fig. 6. (a) Block diagram of a proposed direct-force control system. (b) Schematic diagram of a mass-spring-damper system with an additional pair of spring-damper representing the force sensor.

Based on Fig. 6b, the dynamics of the system becomes an integration between a mass-spring-damper system and a spring-damper system. Hence, the transfer function of the open-loop system is given as

$$G_{Ff} = \frac{K_f}{ms^2 + (b + b_s)s + k + k_s} \tag{9}$$

where K_f denotes the compensation gain for force controller, i.e., from the PC input command to the output analog signal of the F/T sensor. For direct-force control, the transfer function of this closed-loop control system is expressed as

$$\frac{F_a(s)}{F_d(s)} = \frac{K_f K_p (T_d s^2 + s + T_i^{-1})}{ms^3 + (b_t + KK_p T_d)s^2 + (k_t + KK_p)s + KK_p T_i^{-1}} \tag{10}$$

where $F_a(s)$ represents the actual force generated, $X_d(s)$ represents the desired force generated, b_t is the combination of the friction between the F/T sensor and workpiece, and the passive eddy current damping, i.e., $b + b_s$, while k_t is the combination of the stiffness of the flexure-based support bearings and the stiffness of the strain gauge within the F/T sensor, i.e., $k + k_s$.

Using the similar approach in Part A, a comparison between the coefficients of (2) and (10) yields

$$K_p = \frac{m(\omega_n^2 + 2\zeta\omega_n\gamma) - k_t}{K_f} \tag{11}$$

$$T_i = \frac{K_f K_p}{m\gamma\omega_n^2} \tag{12}$$

$$T_d = \frac{m(\gamma + 2\zeta\omega_n) - b_t}{K_f K_p} \tag{13}$$

For the force controller, (11) to (13) are the expressions that describe the three required PID parameters, i.e., K_p, T_i, and T_d. From these expressions, the mass of the moving air-core coil, the stiffness of the flexure-based support bearings, and the passive eddy current damping are known except for the stiffness and damping of the F/T sensor. As a result, a similar empirical approach used in Part A, is adopted to determine these parameters. In this case, an open-loop step response of the FELA is obtained experimentally through a step command input except that the output refers to the single-axis force measurement. The ratio of the output and the input is equivalent to the dc gain of the current closed-loop system. From (9), this dc gain in the steady-state condition is also expressed as

$$DC_{gain} = \frac{K_f}{k + k_s} \tag{14}$$

Based on (9), the output of this transfer function is plotted against the recorded open-loop step response with the assumption that the mass of the air-core coil, the stiffness of the flexure-based support bearings, the passive eddy current damping remain unchanged. The value of the F/T stiffness was initially adjusted to fit the output of (9) to match the actual open-loop step response of the open-loop system as shown in Fig. 7. In this case, the stiffness of the F/T sensor was assumed to be very high while the damping of the sensor is fixed at 1. From Fig. 7, the stiffness was slowly reduced until both data match. Through this empirical approach, the stiffness of the F/T sensor is predicted to be at 1×10^7 N/m. In addition, the compensation gain, K_c , of the current control system is predicted to be 1.054 based on (14).

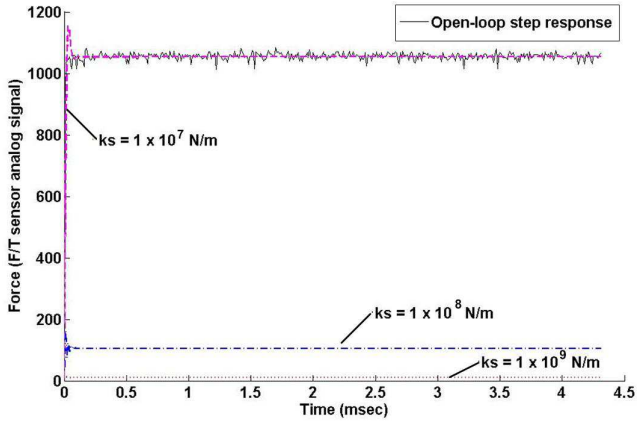

Fig. 7. Open-loop step response and the output of (9) due to the different values of the stiffness of the F/T sensor, while $b_s = 1$.

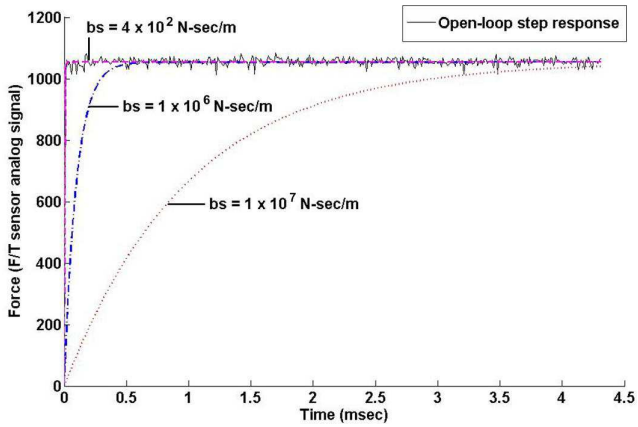

Fig. 8. Open-loop step response and the output of (9) due to the different values of damping of the F/T sensor, while $k_s = 1 \times 10^7$ N/m.

Next, the stiffness of the F/T sensor is fixed at the predicted value while the damping value of the sensor was constantly adjusted to match the output of the transfer function with the actual open-loop step response of the open-loop system as shown in Fig. 8. Using a similar approach, the damping of the F/T sensor was assumed to be very high. From Fig. 8, it shows that the damping value was slowly reduced until the output of transfer function matches the open-loop step response of the system. Eventually, the damping of the F/T sensor is predicted to be 400 N-sec/m. With the values of the stiffness and the damping of the F/T sensor predicted, (11) to (13) are subsequently used to determine the PID parameters. For direct-force control, the settling time is more crucial than the rise time because it will be applied in the imprinting

process. Hence, a settling time of 3 msec and a damping ratio of 0.76 are used in this prediction.

In this section, both PID-based controllers and all PID parameters obtained will be used to form the proposed control schemes. Each control scheme is separately implemented on the FELA to perform a transition between the position control and the direct-force control modes.

V. Comparison Between Both Control Strategies

For the mode-switching control, the position control mode first moved the FELA to its maximum stroke at a velocity of 2 mm/sec before the direct-force control mode takes over with a targeted output force of 30 N once after a contact force was detected. From Fig. 9a, the FELA started moving to its targeted position and stopped its advancement at about 50 μm after a contact force was detected. After switching to the direct-force control mode, the FELA reached the targeted force at 300 msec. However, the sudden surge in command signal caused a sudden pressing effect that is reflected in the force and position profiles at about 140 msec. This sudden surge is caused by the integrator of the force PID controller. In this control scheme, both PID controllers operate simultaneously. When the FELA was operating in the position control mode, the errors built up in the force PID controller as the targeted force was not reached. Subsequently, these accumulated errors caused a surge in the output command signals. Thus, this control scheme loses its effectiveness during the transition between the position control and direct-force control modes.

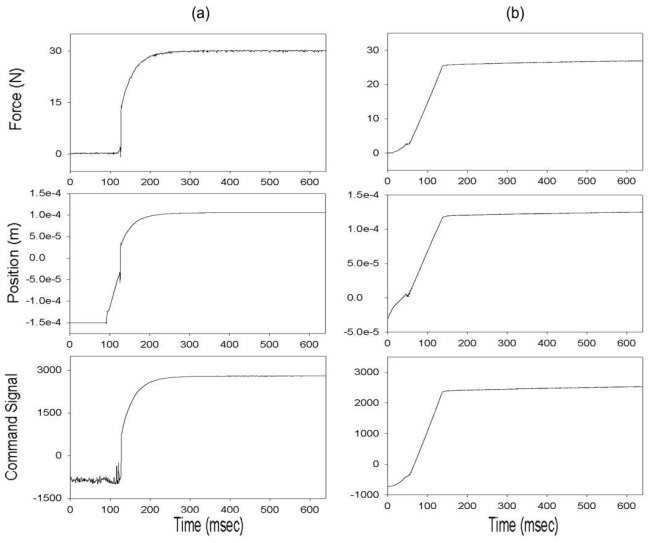

Fig. 9. Force, position and command signal obtained from (a) mode-switching and (b) impedance control modes.

For the impedance control, the position control mode first moved the FELA to its maximum stroke at a velocity of 1 mm/sec before the direct-force control mode took over with a targeted output force of 25 N once after a contact force was detected. From Fig. 9b, the FELA started moving to its targeted position and detected a contact force at about 10 μm. The direct-force control mode then dominated the command signals and operated the FELA to reach its targeted force at about 200 msec. The force output in Fig. 9b suggests that the output force slowly approaches the desired force without any sudden surge. The command signals plot also suggests that this control scheme provides a constant gradient in the command signal which in turn resulted in a smooth transition between the position and force operations. Although mode-switching control offers a more rapid response, such a smooth transition from the impedance control is essential as it prevents the templates or substrates from being damaged during the imprinting processes. Consequently, the impedance method is chosen to realize the hybrid position/force control of a FELA.

VI. Fabrication of Micro-Channels

The desktop hot-embossing imprinter with FELA being set up to realize the hot-embossing process is shown in Fig. 10a. Here, the FELA is fixed vertically downwards with an embossing head mounted on its end-effector. This embossing head, which carries the template (Fig. 10b), has two cartridge heaters for heating up the template. Through the embossing head, the FELA presses the template onto the substrate (Fig. 10c) that is placed on an embossing base. This embossing base has three cartridge heaters for heating up the substrate. All cartridge heaters are designed to heat up the template, and the substrate to 200$^{\circ}C$ within a minute. Temperatures of these cartridge heaters are controlled by the temperature controllers with the thermocouple forming the feedback loop. During the hot-embossing process, the silicon template and the PMMA substrate is heated up to 120$^{\circ}C$ prior to the imprinting. The FELA then carries the template towards the substrate and provides a constant imprinting force of 60 N for five minutes upon contact. Subsequently, the template will be de-molded from the substrate leaving the imprinted micro-channels on the substrate.

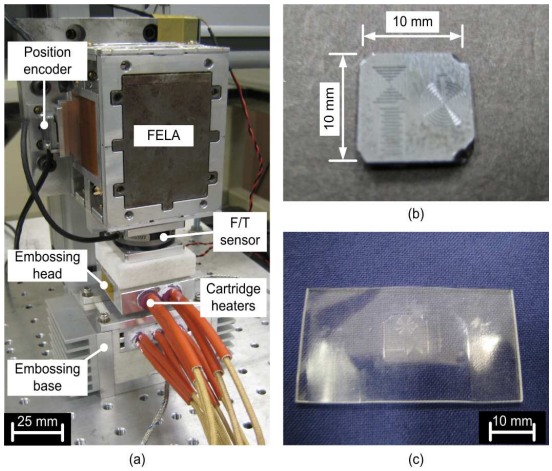

Fig. 10. (a) FELA setup for a hot-embossing process to imprint micro-sized features in (b) the template onto (c) the PMMA substrate.

VII. Experimental Results and Investigations

The imprinted micro-channels on the substrate and the micro-features from the template are taken from a high-

resolution optical microscope, and are shown in Fig. 11. The actual features from the template (Fig. 11b) has a width of 33.3 μm. The imprinted features on the substrate has a measured width of 33.7 μm (Fig. 11a). In addition, the width of a pair of micro-channels from the template is 83.7 μm, while the width of a pair of micro-channels on the substrate is 83.3 μm. Both measurements have shown that the imprinted micro-sized features on the substrate are close to the actual feature from the template with an accuracy of $\pm$0.4 μm.

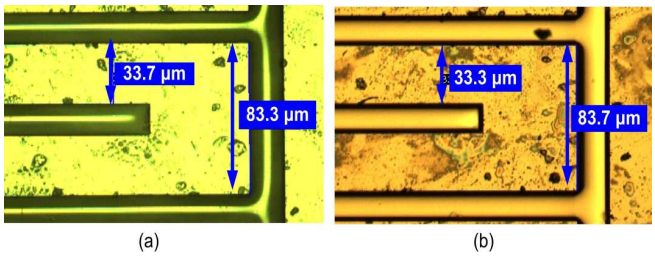

Fig. 11. (a) The imprinted micro-channels on the substrate from (b) the micro-sized features of the template.

After the initial attempt, templates with micro-sized features in a parallel line arrangement have been used for more in-depth evaluations. A total of five templates are used in this evaluation. The parallel lines in each of these templates have specific heights and widths as shown in Table I. According to the measured data, the widths of the micro-channels between the substrates and templates for all five samples are very close. The imprint quality is extremely good in sample 1 and 2 with the widths and heights of the substrates being close to the templates.

TABLE I

MEASUREMENTS OF THE IMPRINTED FEATURES FROM THE SUBSTRATES AND THE TEMPLATES.

	Feature	Silicon template	PMMA
1	Width (μm)	502.0	501.0
	Height (μm)	79.0	78.5
2	Width (μm)	256.5	254.0
	Height (μm)	78.5	76.5
3	Width (μm)	105.5	104.0
	Height (μm)	76.5	71.3
4	Width (μm)	75.5	73.5
	Height (μm)	25.5	13.0
5	Width (μm)	27.5	25.0
	Height (μm)	20.5	10.0

However, it is interesting to note that the imprinted feature height from samples 3 to 5 become shorter than the template feature heights. For example, the variation between the height of the features on sample 3 and from the template was about 6.8% (refer to Table I). These results indicate that the reduction of the width of the template feature increases the difficultly in replicating the height of the template-feature on the substrate. This can be due to the air trapped between the template and the substrate, which hinders the transfer of these features. Hence, this effort has also identified some issues of the hot-embossing process in fabricating features with width size smaller than 100 μm.

VIII. CONCLUSIONS

A high-precision actuator, i.e., FELA, that performs the imprinting task in a desktop-sized hot-embossing imprinter is presented. Modeling of two effective model-based PID controllers to allow the FELA to perform high-precision positioning tasks and direct-force imprinting tasks respectively is discussed in detail. Here, a systematic approach in identifying the unknown physical parameters of FELA is presented and has shown to be an effective tool for system identification. In addition, the performances of two control schemes, i.e., the mode-switching and the impedance control, are investigated and the latter is identified as the most effective control scheme to achieve a smooth imprinting process. With the aid of the impedance control scheme and the model-based PID controllers, the FELA is tasked to automate the imprinting tasks during the fabrication of the micro-channels on PMMA via the hot-embossing process. Results have shown that the features with width size of more than 100 μm can be directly replicated on the substrate. Most importantly, the success of using FELA to automate the required imprinting tasks have shown the efficiency and effectiveness of the implemented impedance control and the two model-based PID controllers.

REFERENCES

[1] C. M. Kiew, W. -J. Lin, T. J. Teo, J. L. Tan, W. Lin and G. L. Yang, "Finite Element Analysis of PMMA Pattern Formation during Hot Embossing Process", *Proc. of IEEE/ASME International Conference on Advance Intelligent Mechatronics*, Singapore, 2009, pp. 314-319.

[2] C. R. Lin, R. H. Chen and C. Hung, The Characterisation and Finite-Element Analysis of a Polymer under Hot Pressing, *International Journal of Advanced Manufacturing Technology*, vol. 20, 2002, pp 230-235.

[3] B. Sprenger, O. Binzel, and R. Siegwart, "Control of A High Performance 3 DOF Linear Direct Drive Operating With Submicron Precision," *4th International Conference on Motion and Vibration Control*, MOVIC '98, Zurich, 1998, pp 1145 - 1150.

[4] K.-S. Chen, D. L. Trumper, and S. T. Smith, "Design and control for an electromagnetically driven X-Y-[theta] stage," *Precision Engineering*, vol. 26, 2002, pp 355-369.

[5] C. Woo Sok and K. Youcef-Toumi, "Modeling of an omni-directional high precision friction drive positioning stage," *Proc. of IEEE International Conference on Robotics and Automation*, vol.1, 1998, pp 175-180.

[6] H. -H. Pham and I. -M. Chen, Stiffness Modeling of Flexure Parallel Mechanism, *Precision Engineering*, vol. 29, 2005, pp 467-478.

[7] J. Lia, R. Sedaghatia, J. Dargahia and D. Waechterb, Design and Development of a New Piezoelectric Linear Inchworm Actuator, *Mechatronics*, vol. 15, 2005, pp 651-681.

[8] Y. Yamagata and T. Higuchi, "A micropositioning device for precision automatic assembly using impact force of piezoelectric elements," *Proc. of IEEE International Conference on Robotics and Automation*, vol.1, 1995, pp 666-671.

[9] T. J. Teo, I. -M. Chen, G. L. Yang and W. Lin, "A Novel Actuator for High-Precision Alignment in Nano-Imprint Multi-Layers-Interconnection Fabrication", *Proc. of IEEE International Conference on Robotics and Automation*, 2007, pp. 1419-1424.

[10] T. J. Teo, I. -M. Chen, G. L. Yang and W. Lin, A Flexure-Based Electromagnetic Linear Actuator, *Nanotechnology*, 2008, vol. 19, pp. 315501-315509.

[11] T. J. Teo, *Flexure-Based Electromagnetic Parallel-Kinematics Manipulator System*, Ph.D. Thesis, Nanyang Technological University (NTU), 2009.

[12] K. Ogata, *Modern Control Engineering*, 4th ed., Prentice Hall; 2001.